

HOW LANDSAT 9 IS SUPERIOR TO LANDSAT 8: COMPARATIVE ASSESSMENT OF LAND USE LAND COVER CLASSIFICATION AND LAND SURFACE TEMPERATURE

F. Ghasempour¹, A. Sekertekin^{2*}, S. H. Kutoglu¹

¹ ZBEU, Engineering Faculty, Geomatics Engineering Department 67100 Zonguldak, Türkiye – (fatemeh.ghasempour, shakan.kutoglu)@beun.edu.tr

² IU, Dept. of Architecture and Town Planning, Iğdır, Türkiye - alihsan_sekertekin@hotmail.com

KEY WORDS: Remote Sensing, LULC, Classification, Random Forest, LST, Landsat 8, Landsat 9.

ABSTRACT:

This study aims (i) to analyze the performance of Landsat 8 and 9's multispectral bands in Land Use Land Cover (LULC) mapping by applying Random Forest (RF) method, and (ii) to compare the LST results of Landsat 8 and 9 using ground-based measurements obtained from Surface Radiation Budget Network (SURFRAD). RF-based classification and pixel-based LST information extraction were conducted in the Google Earth Engine (GEE) environment. Considering the LULC classification, Iğdır province of Türkiye was chosen as the study area, whereas for LST analysis, the location of two SURFRAD stations (FPK and GWN) was selected. Collection 2 Level 2 Surface Reflectance (SR) Products of Landsat 8 and Landsat 9, acquired on 14 May 2022 and 22 May 2022, respectively, were used for LULC mapping. On the other hand, the products of Collection 2 Level 2 Surface Temperature (ST) were utilized for LST analysis. The obtained LULC results showed that Kappa value and Overall Accuracy (OA) for Landsat 9 and Landsat 8 were 87.4 %, 0.83, and 82 %, 0.76, respectively, presenting Landsat 9 achieved better performance in this case study. Concerning the thermal analysis, Landsat 9-based LST provided 1.77 K RMSE, which was lower than Landsat 8-based LST (RMSE=2.31 K). Consequently, Landsat 9 provided better accuracies in both LULC classification and LST analysis, and this study proved that Landsat 9 has more improved OLI and TIRS sensors than Landsat 8.

1. INTRODUCTION

Since the 1950s, the population of the world has risen from 2.5 billion to 7.9 billion, also it is projected to reach 9.7 billion by 2050 (<https://www.macrotrends.net/countries/WLD/world/population>). This growing trend in the population has been leading to demand augmentation for housing, transportation, water, healthcare, food, and energy. To meet these requirements, people have utilized natural resources and caused changes in the Earth's surface (Amini et al., 2022). Thus, generating Land Use Land Cover (LULC) Maps has always been more of an issue for land management, land planning, and sustainable environment (Thiam et al., 2022; Sekertekin et al., 2017). Moreover, the knowledge of the LULC change has usually been critical for many studies (Giuliani et al., 2022), including land use planning (Sakieh et al., 2015), impact assessment on biodiversity (Michelsen, 2008), watershed analyses (Hörmann et al., 2005), and LULC effect on stream ecology (dos Reis Oliveira et al., 2019; Zhou et al., 2012). Therefore, timely, reliable, and accurate LULC knowledge is vital for policy and decision makers to maintain sustainable land resource management. In addition to the LULC mapping, Surface Urban Heat Island (SUHI) effect, which can be extracted from Thermal Infrared (TIR) based images, is another variable for the sustainability of the cities.

Remote Sensing (RS) technology has provided useful information and solutions during the past few decades for monitoring the Earth's surface variations. Satellite imageries have been extensively utilized for the extraction of LULC maps. From the past to the present, various optical RS systems have been launched, some of which are Landsat, Terra/ASTER, SPOT, and Sentinel-2. Among these satellites, Landsat is the unique mission that has been providing images since the 1970s, and the last member of the mission, Landsat 9, was launched on September 27, 2021. Therefore, the number of scientific

publications that used Landsat data has reached a great extent over time (Hemati et al., 2021).

To create an LULC map, a classification method is generally applied to the RS images, and various classification algorithms have been proposed and used so far (Alzubaidi et al., 2021; Khelifi and Mignotte, 2020; Thanh Noi and Kappas, 2017; Korytkowski et al., 2016; Otakei and Blaschke, 2010; Wulder et al., 2008). Concerning the classifiers, Random Forest (RF) has attracted the attention of researchers, and has become one of the widely used methods for LULC mapping thanks to its performance and the demand for a few criteria (Adugna et al., 2022; Balha et al., 2021). On the other hand, SUHI maps can be obtained from TIR-based Land Surface Temperature (LST) images of MODIS, ASTER, Landsat, etc., and various methods have been improved to retrieve TIR-based LST (Gillespie et al., 1998; Qin et al., 2001; Dash et al., 2002; Jiménez-Muñoz and Sobrino, 2003; Sobrino et al., 2004; Duan et al., 2018).

This study aims (i) to compare the performance of Landsat 8 and 9's multispectral bands in LULC mapping using the RF method, and (ii) to compare the LST results of Landsat 8 and 9 using ground-based measurements obtained from Surface Radiation Budget Network (SURFRAD). Furthermore, this is the first study that will provide LST validation of the Landsat 9 TIRS sensor using in-situ measurements. RF-based classification and pixel-based LST information extraction were conducted in the Google Earth Engine (GEE) cloud environment. Although Landsat 9 has similar copies of the Thermal Infrared Sensor (TIRS) and Operational Land Imager (OLI) instruments onboard Landsat 8 as possible, one of the main differences between OLI and OLI-2 instruments is 14 bits of data downloaded per pixel obtaining a higher bit depth for its imagery in comparison with the Landsat 8's

12-bit OLI data

* Corresponding author

(<https://landsat.gsfc.nasa.gov/satellites/landsat-9/landsat-9-instruments/>). On the other hand, The TIRS-2 is an upgraded version of the TIRS-1 from Landsat 8 based on instrument class and stray light reduction (<https://landsat.gsfc.nasa.gov/satellites/landsat-9/landsat-9-instruments/>). That is why we would like to investigate if OLI-2 and TIRS-2's differences(characteristics) have any effect on LULC mapping, and LST analysis, respectively, compared to the OLI-1 and TIRS-1.

2. STUDY AREA AND TEST SITES

2.1 LULC Mapping Study Area

Concerning the LULC mapping, Iğdır Province, located at the Eastern part of Türkiye and along the borders with Iran, Armenia, and Azerbaijan (the area of Nakhchivan Autonomous Republic), was chosen (Figure 1). Iğdır Province is approximately 3588 km² in size, and the height of the city center above the mean sea level is around 850 m. The Iğdir plain is among the most valuable agricultural regions in Turkey, and it has a continental climate; however, lowland parts are not affected by the continental climate as seen in the other parts of Eastern Anatolia due to the micro-climate effect.

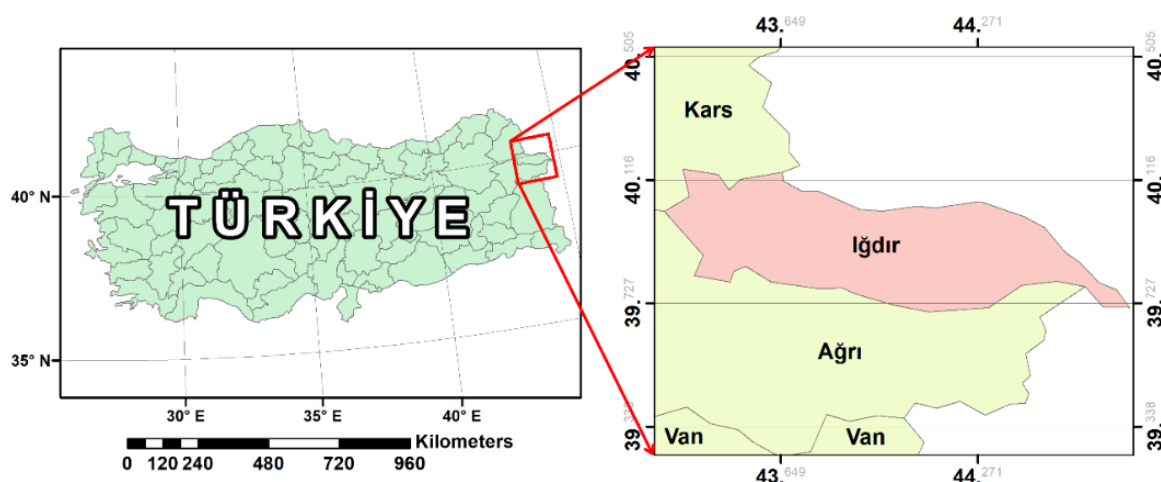


Figure 1. Illustration of the study area map for LULC classification.

2.2 Test Sites for TIRS Comparison

In order to facilitate climate studies across the US, the National Oceanic and Atmospheric Administration (NOAA) of the United States (US) built the SURFRAD network in 1993 by preparing continuous, long period and reliable ground-based data of surface radiation budget (Augustine et al., 2000). Longwave radiation is

one of the parameters that SURFRAD stations measure, and these measurements are used to calculate the ground-based LST. In this study, two SURFRAD stations (FPK and GWN), located at inverse climate zones, were considered for the LST comparisons from TIRS-1 and TIRS-2 (Figure 2).

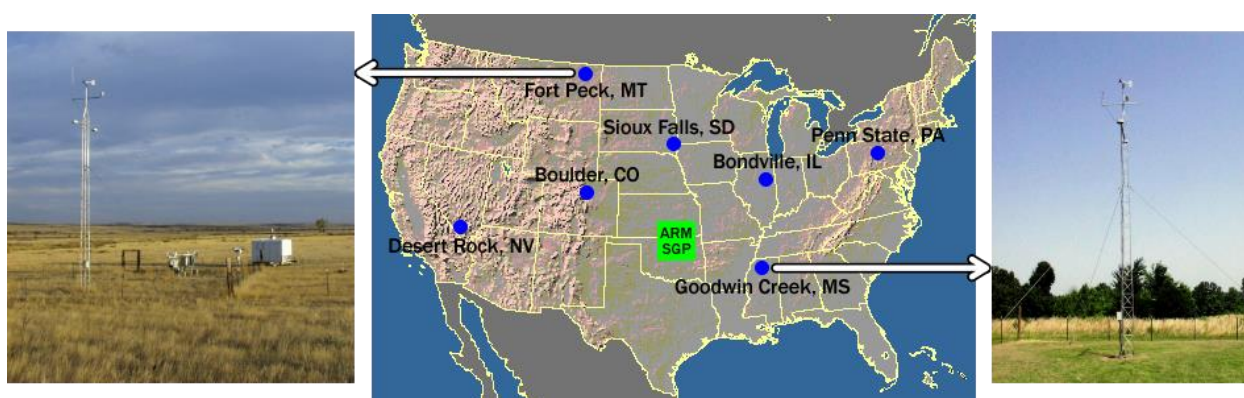


Figure 2. General overview of the SURFRAD network and demonstration of two stations (FPK and GWN) utilized in the LST analysis (Source: <https://www.esrl.noaa.gov/gmd/grad/surfrad/sitepage.html>).

3. DATA AND METHOD

Concerning the LULC mapping, Landsat 8's and Landsat 9's Collection 2 (C2) Level 2 (L2) Surface Reflectance (SR) images (Masek et al., 2006; Vermote et al., 2016) were acquired on 14 May 2022 and 22 May 2022, respectively. Apart from the

panchromatic band, all reflective bands of both datasets were performed in the LULC classification process. In this research, the RF classification method, providing effective performance (Shao et al., 2021), was implemented to identify the LULC classes, namely, water body, vegetation area (pasture, vegetation covered agricultural areas, etc.), artificial surface (urban and

other impervious surfaces), bare land (rocks and bare soils including non-vegetative agricultural lands), and snow cover. The classification process was implemented in the GEE platform. More information about RF can be achieved from the study of Breiman (2001). The number of decision trees (ntree) and the number of variables per split are two significant user-defined factors for the RF, which were defined as 130 and 3, respectively, for this research. Furthermore, for the classification process of each image, 35214 pixels were used in training while 429 pixels were used in testing. To analyze the classification performance, confusion matrix was generated with the Kappa coefficient and Overall Accuracy (OA).

Concerning the LST retrievals, acquisition dates of the Landsat 9 and Landsat 8 images, which are C2 L2 Surface Temperature (ST) Products (Cook, 2014; Cook et al., 2014), are given in the Appendix. The ST products were derived using C2 L1 data, Top of Atmosphere (TOA) reflectance, TOA brightness temperature, atmospheric profile data, and ASTER Global Emissivity Database (GED) data (Cook et al., 2014). To investigate the validation of ST products, two ground-based SURFRAD stations were considered. Many previous studies also utilized SURFRAD in-situ measurements for LST validation (Heidinger et al., 2013; Li et al., 2014; Yu et al., 2014; Zhang et al., 2016; Sekertekin, 2019; Sekertekin and Bonafoni, 2020a, 2020b). To calculate ground-based LST, upwelling and downwelling longwave radiation measurements at two SURFRAD stations were exerted with respect to Stefan–Boltzmann law as in Equation (1) (Li et al., 2014; Wang et al., 2008);

$$LST = \left[\frac{F_{\lambda}^{\uparrow} - (1 - \epsilon_b) \cdot F_{\lambda}^{\downarrow}}{\epsilon_b \cdot \sigma} \right]^{1/4} \quad (1)$$

where F_{λ}^{\uparrow} = upwelling thermal infrared irradiance (W/m²)
 F_{λ}^{\downarrow} = downwelling thermal infrared irradiance (W/m²)
 σ = Stefan-Boltzmann constant
 ϵ_b = broadband longwave surface emissivity

F_{λ}^{\uparrow} and F_{λ}^{\downarrow} are measured simultaneously with satellite pass, and ϵ_b is assumed 0.97.

Landsat-based LST and SURFRAD-derived LST were analyzed considering the performance metrics, namely, average Bias and Root Mean Square Error (RMSE) given by:

$$RMSE = \sqrt{\frac{\sum [T_L - T_{SURFRAD}]^2}{n}} \quad (2)$$

$$Bias = \frac{\sum [T_{SURFRAD} - T_L]}{n} \quad (3)$$

where T_L = Landsat-based LST
 $T_{SURFRAD}$ = SURFRAD-derived LST
 n = the number of data

The general flowchart of the study is in Figure 3, showing all steps including, preprocessing, data, methods, and analysis in the corresponding environment.

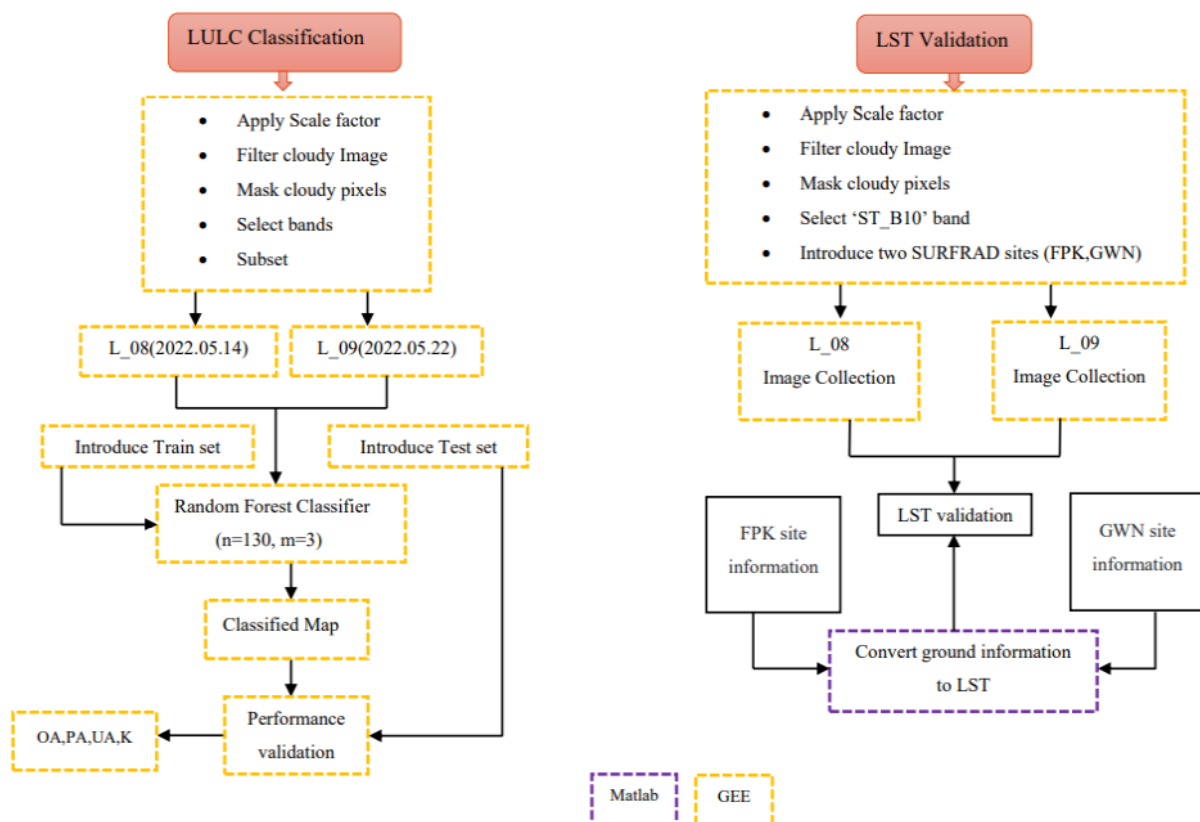


Figure 3. General workflow of this study.

4. RESULTS

Figure 4 represents the RF-based LULC images obtained from Landsat 8 and Landsat 9. For both datasets, the same training and testing data were performed in the classification process. Both

visual interpretation and accuracy metrics revealed that Landsat 9 provided better accuracy than Landsat 8 based on the same training and testing data.

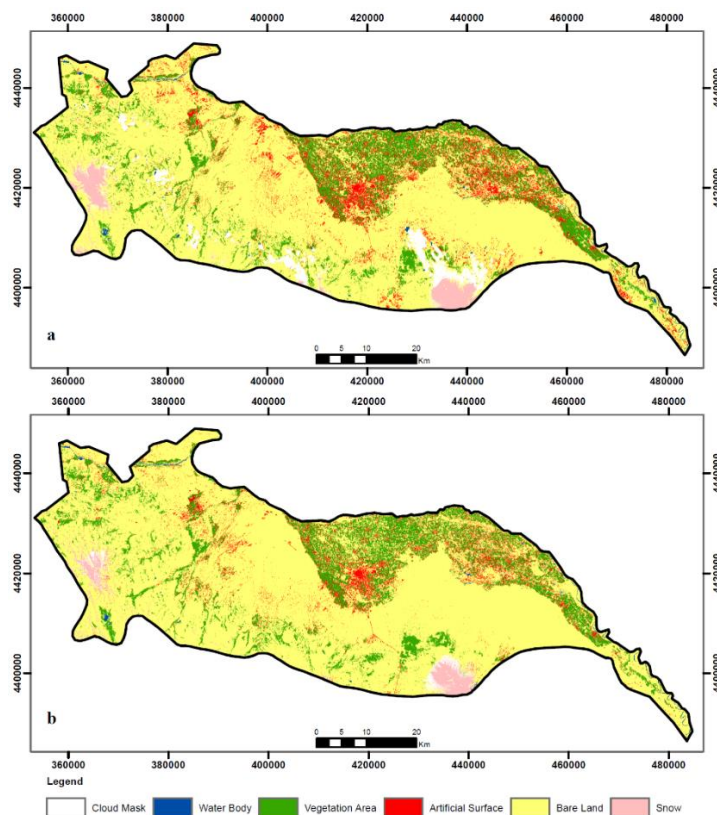


Figure 4. LULC image maps of the interested area; a) Landsat 8 derived LULC, b) Landsat 9 derived LULC.

Table 1 represents the accuracy assessment report for the classification results. The obtained results showed the derived LULC of the Landsat 9 image had a higher kappa value (0.83) and OA (87.4 %) than the Landsat 8-derived LULC (OA=82% and Kappa=0.76). As a visual interpretation, artificial surfaces were better determined by Landsat 9; however, some of the bare lands were identified as artificial surfaces in the Landsat 8-derived LULC image.

Considering the comparison of TIR sensors, Figure 5 represents the LST results from both Landsat images and SURFRAD stations. In-situ LST results from FPK and GWN stations were compared with Landsat 8 and 9 based LST results in Figure 5a and 5b, respectively, while all results from both FPK and GWN stations were presented in Figure 5c. For all scatter plots, Landsat 9-based LST provided slightly better performance than Landsat 8-based LST. It is also required to mention that in this analysis, 27 Landsat 8 images and 19 Landsat 9 images from 2 stations were utilized by considering the clear-sky condition. Over the FPK station, for Landsat 8 and Landsat 9, the RMSE values were 2.60 K and 2.32 K, respectively. Moreover, the average bias was lower for Landsat 9 than Landsat 8. Concerning the GWN station, for Landsat 8 and Landsat 9, the RMSE values were 1.99 K and 1.24 K, respectively. Besides, the average bias was again lower for Landsat 9 than Landsat 8 as in FPK station. For overall evaluation, all data from both FPK and GWN stations were analyzed as seen in Figure 5c. In this general evaluation, Landsat 9-based LST provided 1.77 K RMSE, which was lower than Landsat 8-based LST (RMSE=2.31 K).

LULC Classes	Landsat-8		Landsat-9	
	UA	PA	UA	PA
Snow	1.000	0.889	1.000	1.000
Water Body	0.977	0.860	0.957	0.900
Vegetation Area	0.900	0.771	0.938	0.867
Artificial Surface	0.780	0.742	0.883	0.790
Bare Land	0.745	0.909	0.788	0.932
Overall Accuracy	82 %		87.4 %	
Kappa Coefficient	0.76		0.83	

Table 1. Validation results for LULC images

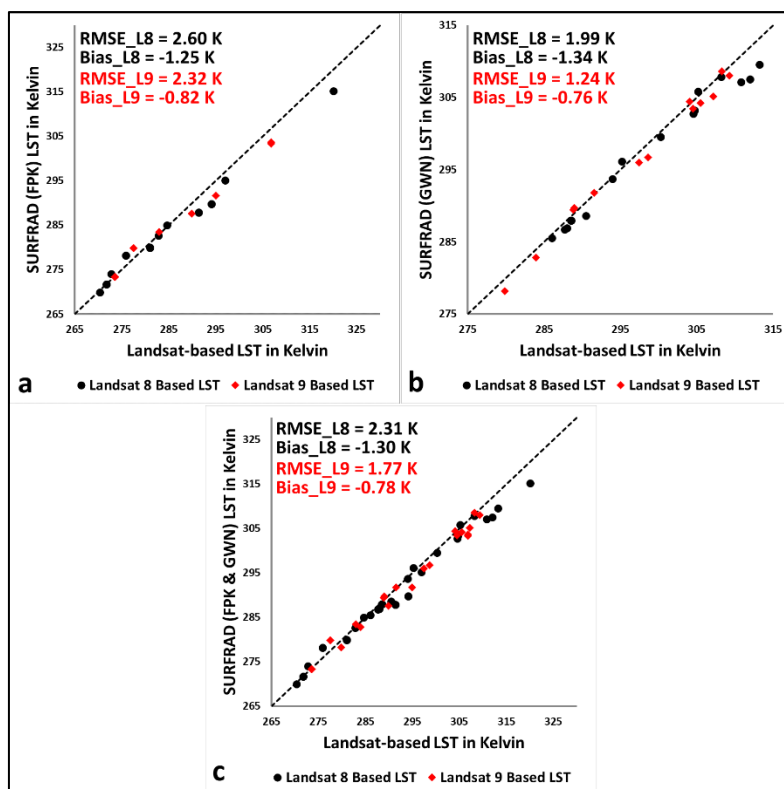


Figure 5. Validations and comparative analysis between Landsat-based LST and SURFRAD-based LST; a) LST results from FPK station, (b) LST results from GWN station, (c) Total LST results from FPK and GWN stations.

5. CONCLUSION

In this study, comparative assessments of Landsat 9 and Landsat 8 were conducted based on LULC classification and LST validation. Thus, the effectiveness of the spectral bands and thermal band (band 10) of both satellite sensors was evaluated. The most recent Landsat satellite is Landsat 9, so we showed its performance on both LULC and LST analysis to highlight the efficiency of OLI-2 and TIRS-2 sensors with a comparative analysis with Landsat 8. For LULC retrieval, the RF method was applied in the GEE cloud platform with the same training and testing data for both Landsat 8 and Landsat 9 images. The LULC results revealed that OA and Kappa values for Landsat 8 and Landsat 9 were 82 %, 0.76, and 87.4 %, 0.83, respectively, presenting that Landsat 9 achieved better performance in this case study. Additionally, regarding the thermal analysis, readily available LST products of Landsat 8 and Landsat 9 from the USGS were evaluated based on ground measurements. FPK and GWN stations from SURFRAD Network were considered in-situ measurement stations. In this analysis, Landsat 9-based LST provided 1.77 K RMSE, which was lower than Landsat 8-based LST (RMSE=2.31 K). As a general evaluation, Landsat 9 provided better accuracies in both LULC classification and LST analysis, and this study proved Landsat 9 has more improved OLI and TIRS sensors than Landsat 8.

ACKNOWLEDGEMENTS

The authors thank the GEE team and platform, USGS, and NASA for enabling a cloud environment for image processing, and providing the Landsat data free of cost, respectively. Moreover, The authors appreciate NOAA's public release of in-situ LST measurements from SURFRAD stations. (<ftp://aftp.cmdl.noaa.gov/data/radiation/surfrad/>).

REFERENCES

- Adugna, T., Xu, W., Fan, J., 2022. Comparison of Random Forest and Support Vector Machine Classifiers for Regional Land Cover Mapping Using Coarse Resolution FY-3C Images. *Remote Sens.* 14, 574. <https://doi.org/10.3390/rs14030574>.
- Alzubaidi, L., Zhang, J., Humaidi, A.J., Al-Dujaili, A., Duan, Y., Al-Shamma, O., Santamaria, J., Fadhel, M.A., Al-Amidie, M., Farhan, L., 2021. Review of deep learning: concepts, CNN architectures, challenges, applications, future directions. *J. Big Data* 8, 53. <https://doi.org/10.1186/s40537-021-00444-8>.
- Amini, S., Saber, M., Rabiei-Dastjerdi, H., Homayouni, S., 2022. Urban Land Use and Land Cover Change Analysis Using Random Forest Classification of Landsat Time Series. *Remote Sens.* 14, 2654. <https://doi.org/10.3390/rs14112654>.
- Augustine, J.A., DeLuisi, J.J., Long, C.N., 2000. SURFRAD—A National Surface Radiation Budget Network for Atmospheric Research. *Bull. Am. Meteorol. Soc.* 81, 2341–2357. [https://doi.org/10.1175/1520-0477\(2000\)081<2341:SANSRB>2.3.CO;2](https://doi.org/10.1175/1520-0477(2000)081<2341:SANSRB>2.3.CO;2).
- Balha, A., Mallick, J., Pandey, S., Gupta, S., Singh, C.K., 2021. A comparative analysis of different pixel and object-based classification algorithms using multi-source high spatial resolution satellite data for LULC mapping. *Earth Sci. Informatics* 14, 2231–2247. <https://doi.org/10.1007/s12145-021-00685-4>.
- Cook, M., 2014. Atmospheric Compensation for a Landsat Land

- Surface Temperature Product. Thesis, Rochester Institute of Technology.
- Cook, M., Schott, J., Mandel, J., Raqueno, N., 2014. Development of an Operational Calibration Methodology for the Landsat Thermal Data Archive and Initial Testing of the Atmospheric Compensation Component of a Land Surface Temperature (LST) Product from the Archive. *Remote Sens.* 6, 11244–11266. <https://doi.org/10.3390/rs6111244>.
- Dash, P., Göttsche, F.-M., Olesen, F.-S., Fischer, H., 2002. Land surface temperature and emissivity estimation from passive sensor data: Theory and practice-current trends. *Int. J. Remote Sens.* 23, 2563–2594. <https://doi.org/10.1080/01431160110115041>
- dos Reis Oliveira, P.C., van der Geest, H.G., Kraak, M.H.S., Verdonshot, P.F.M., 2019. Land use affects lowland stream ecosystems through dissolved oxygen regimes. *Sci. Rep.* 9, 19685. <https://doi.org/10.1038/s41598-019-56046-1>.
- Duan, S.-B., Li, Z.-L., Wang, C., Zhang, S., Tang, B.-H., Leng, P., Gao, M.-F., 2018. Land-surface temperature retrieval from Landsat 8 single-channel thermal infrared data in combination with NCEP reanalysis data and ASTER GED product. *Int. J. Remote Sens.* 40(5-6), 1–16. <https://doi.org/10.1080/01431161.2018.1460513>.
- Gillespie, A., Rokugawa, S., Matsunaga, T., Steven Cothorn, J., Hook, S., Kahle, A.B., 1998. A temperature and emissivity separation algorithm for advanced spaceborne thermal emission and reflection radiometer (ASTER) images. *IEEE Trans. Geosci. Remote Sens.* 36, 1113–1126. <https://doi.org/10.1109/36.700995>.
- Giuliani, G., Rodila, D., Külling, N., Maggini, R., Lehmann, A., 2022. Downscaling Switzerland Land Use/Land Cover Data Using Nearest Neighbors and an Expert System. *Land* 11, 615. <https://doi.org/10.3390/land11050615>.
- Heidinger, A.K., Laszlo, I., Molling, C.C., Tarpley, D., 2013. Using SURFRAD to verify the NOAA single-channel land surface temperature algorithm. *J. Atmos. Ocean. Technol.* 30, 2868–2884. <https://doi.org/10.1175/JTECH-D-13-00051.1>.
- Hemati, M., Hasanlou, M., Mahdianpari, M., Mohammadimanesh, F., 2021. A Systematic Review of Landsat Data for Change Detection Applications: 50 Years of Monitoring the Earth. *Remote Sens.* 13, 2869. <https://doi.org/10.3390/rs13152869>.
- Hörmann, G., Horn, A., Fohrer, N., 2005. The evaluation of land-use options in mesoscale catchments. *Ecol. Modell.* 187, 3–14. <https://doi.org/10.1016/j.ecolmodel.2005.01.022>.
- Jiménez-Muñoz, J.C., Sobrino, J.A., 2003. A generalized single-channel method for retrieving land surface temperature from remote sensing data. *J. Geophys. Res.* 109, 8112. <https://doi.org/10.1029/2004JD004804>.
- Khelifi, L., Mignotte, M., 2020. Deep Learning for Change Detection in Remote Sensing Images: Comprehensive Review and Meta-Analysis. *IEEE Access* 8, 126385–126400. <https://doi.org/10.1109/ACCESS.2020.3008036>.
- Korytkowski, M., Rutkowski, L., Scherer, R., 2016. Fast image classification by boosting fuzzy classifiers. *Inf. Sci.* 327, 175–182. <https://doi.org/10.1016/j.ins.2015.08.030>.
- Li, H., Sun, D., Yu, Y., Wang, Hongyan, Liu, Y., Liu, Q., Du, Y., Wang, Heshun, Cao, B., 2014. Evaluation of the VIIRS and MODIS LST products in an arid area of Northwest China. *Remote Sens. Environ.* 142, 111–121. <https://doi.org/10.1016/j.rse.2013.11.014>.
- Masek, J.G., Vermote, E.F., Saleous, N.E., Wolfe, R., Hall, F.G., Huemmrich, K.F., Gao, F., Kutler, J., Lim, T.-K., 2006. A Landsat Surface Reflectance Dataset for North America, 1990–2000. *IEEE Geosci. Remote Sens. Lett.* 3, 68–72. <https://doi.org/10.1109/LGRS.2005.857030>.
- Michelsen, O., 2008. Assessment of land use impact on biodiversity. *Int. J. Life Cycle Assess.* 13, 22–31. <https://doi.org/10.1065/lca2007.04.316>.
- Otukei, J.R., Blaschke, T., 2010. Land cover change assessment using decision trees, support vector machines and maximum likelihood classification algorithms. *Int. J. Appl. Earth Obs. Geoinf.* 12, 27–31. <https://doi.org/10.1016/j.jag.2009.11.002>.
- Qin, Z., Karnieli, A., Berliner, P., 2001. A mono-window algorithm for retrieving land surface temperature from Landsat TM data and its application to the Israel-Egypt border region. *Int. J. Remote Sens.* 22, 3719–3746. <https://doi.org/10.1080/01431160010006971>.
- Sakieh, Y., Salmanmahiny, A., Jafarnezhad, J., Mehri, A., Kamyab, H., Galdavi, S., 2015. Evaluating the strategy of decentralized urban land-use planning in a developing region. *Land use policy* 48, 534–551. <https://doi.org/10.1016/j.landusepol.2015.07.004>.
- Sekertekin, A., 2019. Validation of Physical Radiative Transfer Equation-Based Land Surface Temperature Using Landsat 8 Satellite Imagery and SURFRAD in-situ Measurements. *J. Atmos. Solar-Terrestrial Phys.* 196. <https://doi.org/10.1016/j.jastp.2019.105161>.
- Sekertekin, A., Bonafoni, S., 2020a. Land Surface Temperature Retrieval from Landsat 5, 7, and 8 over Rural Areas: Assessment of Different Retrieval Algorithms and Emissivity Models and Toolbox Implementation. *Remote Sens.* 12, 294. <https://doi.org/10.3390/rs12020294>.
- Sekertekin, A., Bonafoni, S., 2020b. Sensitivity Analysis and Validation of Daytime and Nighttime Land Surface Temperature Retrievals from Landsat 8 Using Different Algorithms and Emissivity Models. *Remote Sens.* 12, 2776. <https://doi.org/10.3390/rs12172776>.
- Sekertekin, A., Marangoz, A.M., Akcin, H., 2017. Pixel-based classification analysis of land use land cover using Sentinel-2 and Landsat-8 data. *Int. Arch. Photogramm. Remote Sens. Spatial Inf. Sci.*, XLII-4/W6, 91–93. <https://doi.org/10.5194/isprs-archives-XLII-4-W6-91-2017>.
- Shao, Z., Sumari, N.S., Portnov, A., Ujoh, F., Musakwa, W., Mandela, P.J., 2021. Urban sprawl and its impact on sustainable urban development: a combination of remote sensing and social media data. *Geo-spatial Inf. Sci.* 24, 241–255. <https://doi.org/10.1080/10095020.2020.1787800>.

Sobrino, J.A., Jiménez-Muñoz, J.C., Paolini, L., 2004. Land surface temperature retrieval from LANDSAT TM 5. *Remote Sens. Environ.* 90, 434–440. <https://doi.org/10.1016/j.rse.2004.02.003>.

Thanh Noi, P., Kappas, M., 2017. Comparison of Random Forest, k-Nearest Neighbor, and Support Vector Machine Classifiers for Land Cover Classification Using Sentinel-2 Imagery. *Sensors* 18(1), 18. <https://doi.org/10.3390/s18010018>.

Thiam, S., Salas, E.A.L., Houngouè, N.R., Almoradie, A.D.S., Verleysdonk, S., Adoukpe, J.G., Komi, K., 2022. Modelling Land Use and Land Cover in the Transboundary Mono River Catchment of Togo and Benin Using Markov Chain and Stakeholder's Perspectives. *Sustainability* 14, 4160. <https://doi.org/10.3390/su14074160>.

Vermote, E., Justice, C., Claverie, M., Franch, B., 2016. Preliminary analysis of the performance of the Landsat 8/OLI land surface reflectance product. *Remote Sens. Environ.* 185, 46–56. <https://doi.org/10.1016/j.rse.2016.04.008>.

Wang, W., Liang, S., Meyers, T., 2008. Validating MODIS land surface temperature products using long-term nighttime ground measurements. *Remote Sens. Environ.* 112, 623–635. <https://doi.org/10.1016/j.rse.2007.05.024>.

Wulder, M.A., White, J.C., Goward, S.N., Masek, J.G., Irons, J.R., Herold, M., Cohen, W.B., Loveland, T.R., Woodcock, C.E., 2008. Landsat continuity: Issues and opportunities for land cover monitoring. *Remote Sens. Environ.* 112, 955–969. <https://doi.org/10.1016/j.rse.2007.07.004>.

Yu, X., Guo, X., Wu, Z., 2014. Land surface temperature retrieval from landsat 8 TIRS-comparison between radiative transfer equation-based method, split window algorithm and single channel method. *Remote Sens.* 6, 9829–9852. <https://doi.org/10.3390/rs6109829>.

Zhang, Z., He, G., Wang, M., Long, T., Wang, G., Zhang, X., 2016. Validation of the generalized single-channel algorithm using landsat 8 imagery and SURFRAD ground measurements. *Remote Sens. Lett.* 7, 810–816. <https://doi.org/10.1080/2150704X.2016.1190475>.

Zhou, T., Wu, J., Peng, S., 2012. Assessing the effects of landscape pattern on river water quality at multiple scales: A case study of the Dongjiang River watershed, China. *Ecol. Indic.* 23, 166–175. <https://doi.org/10.1016/j.ecolind.2012.03.013>.

APPENDIX

Station Id	Acquisition Dates (dd.mm.yyyy)	
	Landsat 8	Landsat 9
FPK	1.11.2021	10.11.2021
	8.11.2021	13.2.2022
	17.11.2021	24.3.2022
	3.12.2021	18.4.2022
	12.2.2022	25.4.2022
	9.3.2022	4.5.2022
	16.3.2022	
	25.3.2022	
	26.4.2022	
	19.5.2022	
GWN	6.11.2021	23.12.2021
	13.11.2021	17.1.2022
	22.11.2021	24.1.2022
	29.11.2021	9.2.2022
	8.12.2021	18.2.2022
	25.1.2022	7.4.2022
	10.2.2022	14.4.2022
	14.3.2022	30.4.2022
	15.4.2022	16.5.2022
	22.4.2022	26.6.2022
	1.5.2022	12.7.2022
	8.5.2022	19.7.2022
	18.6.2022	28.7.2022
25.6.2022		
11.7.2022		
20.7.2022		